



Monolithic color-selective ultraviolet (266–315nm) photodetector based on a wurtzite $\text{Mg}_x\text{Zn}_{1-x}\text{O}$ film

Y. N. Hou, Z. X. Mei, H. L. Liang, C. Z. Gu, and X. L. Du

Citation: [Applied Physics Letters](#) **105**, 133510 (2014); doi: 10.1063/1.4897300

View online: <http://dx.doi.org/10.1063/1.4897300>

View Table of Contents: <http://scitation.aip.org/content/aip/journal/apl/105/13?ver=pdfcov>

Published by the [AIP Publishing](#)

Articles you may be interested in

[Energy-selective multichannel ultraviolet photodiodes based on \(Mg,Zn\)O](#)

Appl. Phys. Lett. **103**, 171111 (2013); 10.1063/1.4826596

[The effect of oxygen flow rate and radio frequency plasma power on cubic ZnMgO ultraviolet sensors grown by plasma-enhanced molecular beam epitaxy](#)

Appl. Phys. Lett. **103**, 031114 (2013); 10.1063/1.4815995

[Mott-type \$\text{Mg}_x\text{Zn}_{1-x}\text{O}\$ -based visible-blind ultraviolet photodetectors with active anti-reflection layer](#)

Appl. Phys. Lett. **102**, 231122 (2013); 10.1063/1.4811153

[Mg x Zn 1 x O -based photodetectors covering the whole solar-blind spectrum range](#)

Appl. Phys. Lett. **93**, 173505 (2008); 10.1063/1.3002371

[Compositionally-tuned epitaxial cubic Mg x Zn 1x O on Si\(100\) for deep ultraviolet photodetectors](#)

Appl. Phys. Lett. **82**, 3424 (2003); 10.1063/1.1576309

The logo for AIP Chaos is displayed in a white font on a red background. The letters 'AIP' are large and bold, followed by a vertical bar and the word 'Chaos' in a smaller font.

AIP | Chaos

CALL FOR APPLICANTS
Seeking new Editor-in-Chief

Monolithic color-selective ultraviolet (266–315 nm) photodetector based on a wurtzite $\text{Mg}_x\text{Zn}_{1-x}\text{O}$ film

Y. N. Hou, Z. X. Mei,^{a)} H. L. Liang, C. Z. Gu, and X. L. Du^{a)}

Beijing National Laboratory for Condensed Matter Physics, Institute of Physics, Chinese Academy of Sciences, Beijing 100190, China

(Received 31 July 2014; accepted 20 September 2014; published online 1 October 2014)

A unique ultraviolet photodetector based on a metal-semiconductor-metal structure was fabricated from a wurtzite $\text{Mg}_x\text{Zn}_{1-x}\text{O}$ film with gradually changing Mg content, homoepitaxially grown on a BeO-buffered ZnO substrate. The BeO layer filtered out the substrate photoresponse. The cutoff wavelength of the photodetector under zero bias was 266 nm with a UV/visible light rejection ratio of greater than 2 orders of magnitude in the deep UV region. Applying a bias, the cutoff wavelength exhibited a prominent continuous redshift from 266 (0 V) to 315 nm (3 V), indicating the capability for multi-band UV detection on a monolithic chip. The bias-controlled wavelength-selective UV photoresponse mechanism occurred in the optically active area in a compositionally distributed $\text{Mg}_x\text{Zn}_{1-x}\text{O}$ alloy that was achieved by molecular epitaxial growth. © 2014 AIP Publishing LLC. [<http://dx.doi.org/10.1063/1.4897300>]

Ultraviolet (UV) detection based on wide-band-gap (E_g) semiconductors has tremendous potential for military and commercial applications such as for early warning of missile plumes, secure communication, medical instruments, air/water purification, and photolithography.^{1–3} The large, magnified E_g allows UV photodetectors (PDs) to operate under a visible light background without unwieldy optical filters and cooling hardware, which are typically used in traditional UV detectors. These traditional UV detectors have serious compatibility issues with modern compact circuits.⁴ Among various wide-band-gap semiconductors, $\text{Mg}_x\text{Zn}_{1-x}\text{O}$ alloys are a class of excellent materials with tunable E_g values in the range of 3.37–7.8 eV for the fabrication of high-performance wavelength-selective UV PDs.⁵ The tunability of the energy band gap over such a wide range allows the fabrication of multi-waveband UV PDs, which are needed for multi-signal processing in devices being designed in the fast-developing field of optoelectronic information technology.⁶ In previous work, multi-wavelength UV PDs were designed by depositing a number of electrodes on optically active regions (OARs). The electrodes were distributed laterally on a wafer, by using pulsed laser deposition over a selected area.^{7–9} Thus, the response wavelength was determined by the position of the electrodes, making it difficult to scale down the size of such UV PDs with the corresponding integrated circuits. In addition, these detectors were not able to detect deep UV light because they were restricted by the Mg content applied.^{7–9}

Owing to a phase separation problem in $\text{Mg}_x\text{Zn}_{1-x}\text{O}$, which is caused by the difference between the binding components ZnO and MgO (both in the coordination structure of the lattice and the configurational entropy of the chemical bond), the synthesis of single-phase wurtzite $\text{Mg}_x\text{Zn}_{1-x}\text{O}$ with a high Mg content is not trivial.¹⁰ Unique interface engineering has been exploited to gradually improve the phase

separation limit and the performance of $\text{Mg}_x\text{Zn}_{1-x}\text{O}$ PDs.^{11–15} In the present work, we report a paradigm change in PD innovation in the form of a multi-waveband UV PD constructed on a single-phase $\text{Mg}_x\text{Zn}_{1-x}\text{O}$ film. The UV PD is homoepitaxially grown on a ZnO substrate buffered by a thin film of BeO. The UV PD is configured in a metal-semiconductor-metal (MSM) geometry with Ti/Au Schottky electrodes. The device performance was evaluated by measuring its optoelectronic properties. The photoresponsivity spectra demonstrated that the long wavelength photoresponse from the ZnO substrate was fully eliminated by using BeO, which acted as an electron blocking filter. The cutoff wavelength at 0 V was discovered to be 266 nm with a UV-to-visible light rejection ratio of greater than 2 orders of magnitude. Applying a bias, the cutoff underwent a continuous redshift from 266 nm (0 V) to 315 nm (3 V), indicating that our UV PD was able to detect UV radiation across multiple wavebands. The working principle of the device is proposed and verified by simulations.

The core of the device was made of unintentionally doped $\text{Mg}_x\text{Zn}_{1-x}\text{O}$ films, which were grown on a ZnO substrate using a plasma-assisted molecular beam epitaxy (rf-MBE) equipped with high purity Zn, Mg, and oxygen plasma sources. First, a 30-nm-thick BeO layer was deposited on the pretreated ZnO substrate at 850 °C, making a good template for $\text{Mg}_x\text{Zn}_{1-x}\text{O}$ epitaxy. Its insulating shield prevents carriers that are photo-generated in the ZnO substrate from drifting into the active $\text{Mg}_x\text{Zn}_{1-x}\text{O}$ layer.¹⁶ Following this step, 20 nm of low Mg content $\text{Mg}_x\text{Zn}_{1-x}\text{O}$ was grown at 450 °C and annealed at 750 °C for 10 min to serve as the “quasi-homo buffer.”¹¹ Then, the graded $\text{Mg}_x\text{Zn}_{1-x}\text{O}$ epitaxial layer with a thickness of 350 nm was grown at 450 °C. The Mg content was gradually increased along the *c* axis (growth direction) by controlling the Mg:Zn flux ratio from 0.63 to 0.88. The epitaxial structure is schematically shown in Fig. 1(a). During the entire growth procedure, the sample was monitored using *in situ* reflection high-energy electron diffraction (RHEED). The distinct RHEED diffraction

^{a)}Authors to whom correspondence should be addressed. Electronic addresses: zxmei@aphy.iphy.ac.cn and xldu@aphy.iphy.ac.cn.

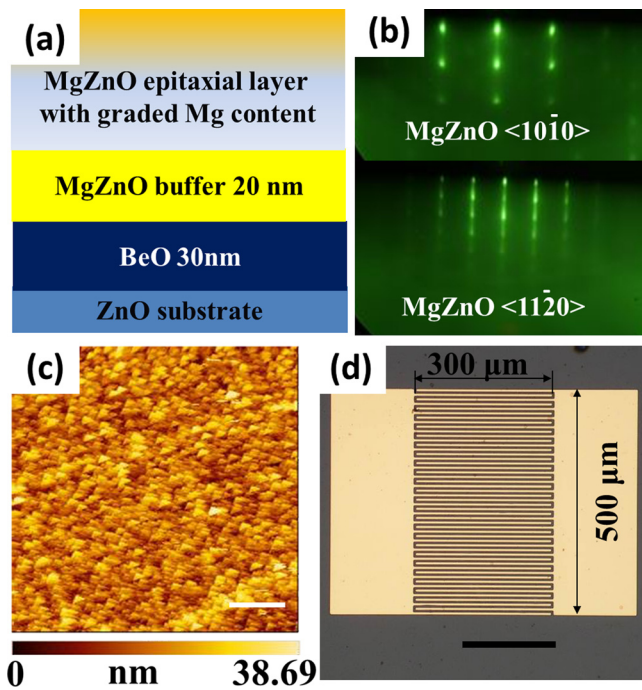


FIG. 1. (a) Schematic diagram of the epilayers, (b) RHEED diffraction patterns of the $\text{Mg}_x\text{Zn}_{1-x}\text{O}$ epilayer, (c) AFM image of the MgZnO surface scanned over a $10 \times 10 \mu\text{m}^2$ area (scale bar = $2 \mu\text{m}$), and (d) the top view of the PD from an optical microscope (scale bar = $200 \mu\text{m}$).

patterns from the planes $\langle 11-20 \rangle$ and $\langle 10-10 \rangle$ indicate the high crystallinity and flat surface of the epitaxial film, as shown in Fig. 1(b). The surface morphology was further evaluated using atomic force microscopy (AFM). The obtained root mean square roughness of 1.87 nm in a $10 \times 10 \mu\text{m}^2$ scanning area additionally demonstrates a high flatness of the surface (Fig. 1(c)), consistent with the *in situ* RHEED observations. The UV PDs were fabricated by conventional photolithography and lift-off processes. Ti/Au ($10/50 \text{ nm}$) contacts of each PD were defined as interdigital MSM structures, which are believed to possess a low parasitic capacitance, with fingers $300 \mu\text{m}$ in length and $5 \mu\text{m}$ in width spaced by a $5 \mu\text{m}$ gap (Fig. 1(d)). The current-voltage (I-V) measurement was characterized using a Keithley 6487 picoammeter (Keithley Instruments, Inc.). The photoresponse and photocurrent were measured using a 75 W xenon lamp, followed by a 0.5-m high-resolution monochromator (SpectraPro-500i, Acton Research Corporation) as the illumination source.

Fig. 2 shows the dark I-V characteristics of our multi-waveband UV PD from -3 V to 3 V . A clear rectification behavior with an exponential relationship between the current and the applied voltage was observed, indicating the typical back-to-back Schottky property of the contact. The dark current at $\pm 3 \text{ V}$ is less than 10 nA , corresponding to a current density of $1.3 \times 10^{-5} \text{ A/cm}^2$, considering the contact area. This low dark current demonstrates the high quality of the $\text{Mg}_x\text{Zn}_{1-x}\text{O}$ homoepitaxially grown on the ZnO substrate. The inset of Fig. 2 displays a single junction Schottky diode fabricated on the same film. By fitting the curve with Richardson-Dushman relationship, the Schottky barrier height and ideality factor were estimated as 0.64 eV and 25 , respectively. The large Schottky barrier height is due to

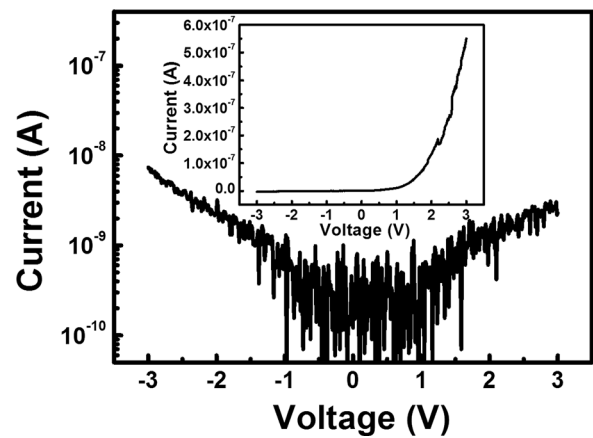


FIG. 2. The I-V characterization of the MSM PD. (The inset provides the I-V curve of a single Schottky junction diode fabricated on the same epilayer.)

Mg's $3s$ -electron bonding with oxygen atoms, which greatly increases the conduction band minimum,¹³ whereas the large ideality factor results from the extensive series resistance of the undoped $\text{Mg}_x\text{Zn}_{1-x}\text{O}$.

The spectrum response under zero bias is shown in Fig. 3(a). The cutoff wavelength was observed at 266 nm in the deep UV region with a photoresponsivity of 10 mA/W , corresponding to a detectivity of approximately $2 \times 10^8 \text{ Hz}^{1/2} \text{ cm}^{-1}$. The UV-to-visible rejection ratio is greater than 2 orders of magnitude, indicating a high signal-to-noise ratio. The photocurrent spectra under different applied biases are exhibited in Fig. 3(b). Clearly, the peak value of the photocurrent increases exponentially with applied bias (Fig. 3(c), red line with filled circles), indicating a large internal gain. The cutoff wavelength against applied bias is also plotted in Fig. 3(c) (blue line with filled squares). The cutoff wavelength shows a continuous redshift from 266 nm (in the deep UV-C region) under zero bias to 315 nm (in the UV-B region) under 3 V , suggesting the realization of a multi-waveband UV detector on a monolithic chip. The working principle of this type of multi-waveband UV PD will be illustrated later in this study using electric field analysis.

The setup of the temporal photoresponse measurement is schematically shown in the inset of Fig. 3(d). The UV PD was biased using a Keithley 6487 voltage source and was exposed to a periodic 254-nm UV illumination. The photocurrent signal was monitored by recording the voltage on a $100\text{-K}\Omega$ load resistor with a Tektronix TD1012B oscilloscope. As shown in Fig. 3(d), the decay time of the UV PD exhibits a rapid decreased followed by a long tail. The transient photoresponse behavior was studied by fitting the curve with a biexponential decay function

$$I = I_1 \cdot \exp(-t/\tau_1) + I_2 \cdot \exp(-t/\tau_2), \quad (1)$$

where I and t are the intensity of the UV response signal and time and τ_1 and τ_2 are the fast and slow decay times, respectively. The fast and slow decay times are 5.5 s and 66.0 s , respectively. This slow response time makes it difficult for the photocurrent to recover to the initial value after UV illumination, namely, the persistent photocurrent (PPC), which is frequently observed in ZnO-based materials. Normally, the direct recombination of the electron-hole in MgZnO is of

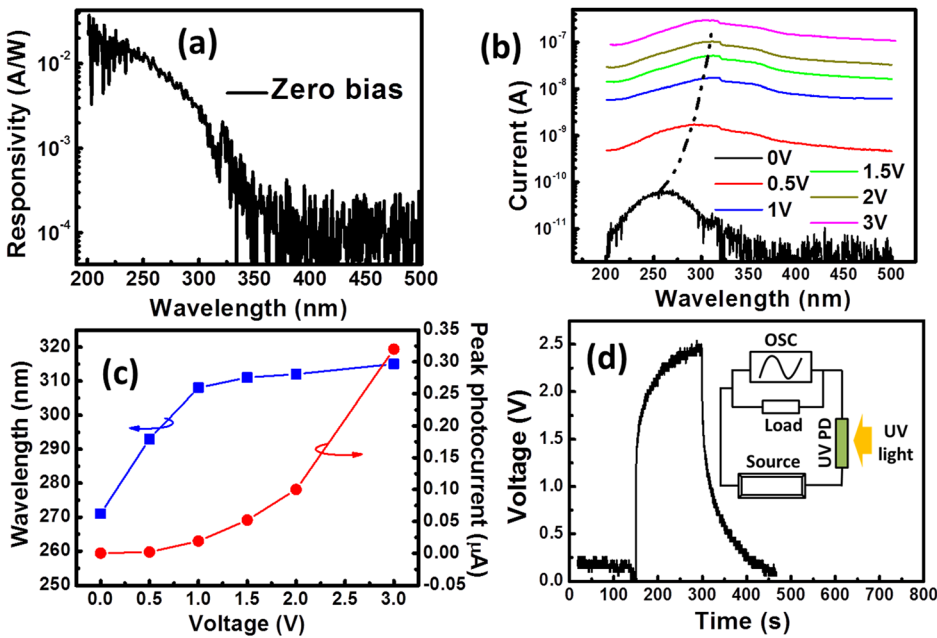


FIG. 3. (a) The response spectrum of the PD at 0V, (b) the peak of photocurrent spectra shows a clear redshift from 0V to 3V (the dashed line is a guide), (c) the cutoff wavelength and the peak photocurrent plotted as a function of the applied voltage, and (d) the transient response of the PD. (The inset shows the configuration of the transient response measurement system.)

the order of picoseconds,¹⁷ much faster than our observations. In this context, the long lifetime of our device can reasonably be attributed to the presence of oxygen vacancies (V_o), which are a common, intrinsic deep level defect in ZnO-related materials formed during epitaxial growth.¹⁸ Under UV illumination, V_o will transition to its charged states, V_o^+ or V_o^{++} , and release conducting electrons. However, after illumination, these charged states relax back to their neutral states only with difficulty, owing to the lattice deformation potential induced by the ionization process, causing a clear PPC.¹⁹

To understand the multi-waveband detection behavior of our UV PD, the depth of OAR was analyzed using a simulation of the electric field distribution under increasing bias with a finite element method. The dielectric permittivity used for the simulation is 10, which has been evaluated in our previous reports.¹⁵ The results of the simulations are shown in Figs. 4(a)–4(c). The band gap of $Mg_xZn_{1-x}O$ is known to increase almost linearly with Mg content, ignoring the bowing parameter, and can be expressed by

$$E_g^{(MgZnO)} = x \cdot E_g^{(ZnO)} + (1 - x) \cdot E_g^{(MgO)}, \quad (2)$$

where the $E_g^{(MgZnO)}$, $E_g^{(ZnO)}$, and $E_g^{(MgO)}$ represent the band gap of $Mg_xZn_{1-x}O$, ZnO, and wurtzite MgO (band gap of ~ 6.3 eV),²⁰ respectively. In this case, the band gap of our thin film gradually increases along the growth direction (c axis) by the aforementioned control of the Mg content during growth. When the device is placed under a low bias, the electric field is mainly distributed near the surface, i.e., the OAR is located at a relatively larger band gap region (Fig. 4(a)). The electrons and holes generated by deep UV illumination of the upper layer readily drift to the electrodes under the electric field, resulting in a deep UV photoresponse. However, the photon-generated electrons and holes rapidly recombine because they are not covered by the OAR in the region underneath. Similarly, the OAR gradually stretches into $Mg_xZn_{1-x}O$ with a lower Mg content when the bias is increased. From the simulation, the electric field depth significantly increases 6-fold at 3V (Fig. 4(c)) compared with that at 0.5V (Fig. 4(a)). In this situation, photoresponsivity

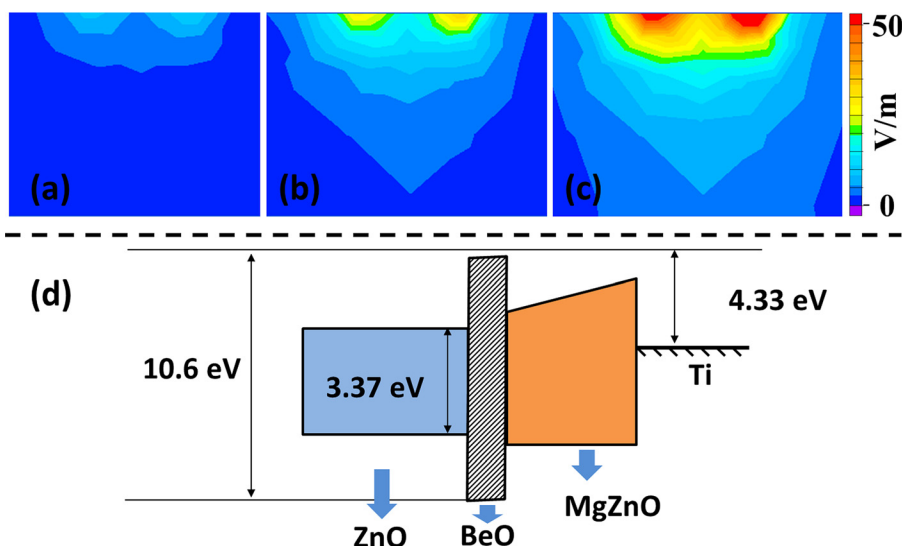


FIG. 4. Simulation of the electric field distribution under (a) 0.5 V, (b) 1.5 V, (c) 3 V, and (d) a schematic diagram of the band structure of the PD.

from the low Mg region occurs. No photoresponse from the ZnO substrate was observed due to the 30-nm BeO electron-blocking layer. As shown in Fig. 4(d), the band diagram of the PD is drawn according to the Schokley-Mott model. The band gaps of ZnO and BeO are 3.37 and 10.6 eV, respectively, and the electron affinities of ZnO and BeO are 4.3 and 0.5 eV, respectively.^{21,22} Large conduction and valence band offsets form at the ZnO/BeO interface. As a result, the photo-generated carriers in the ZnO substrate cannot overcome barriers to induce an effective photoresponse, causing only the response from the epilayers to remain.

In conclusion, a type of MSM UV PD was fabricated from a homoepitaxially grown $\text{Mg}_x\text{Zn}_{1-x}\text{O}$ film with a graded Mg content. By controlling the applied bias, the cut-off wavelength of the UV PD can be modulated from 315 nm to 266 nm with a UV/visible light rejection ratio of 2 orders of magnitude, achieving selective multi-waveband detection from visible-blind to the deep UV region on a monolithic chip. The OAR is distributed in the high Mg content region of $\text{Mg}_x\text{Zn}_{1-x}\text{O}$ at low voltages and in the low Mg content region of $\text{Mg}_x\text{Zn}_{1-x}\text{O}$ at high voltages, which is in good agreement with the simulation. This behavior is considered as the principle of our wavelength-selective UV PD. We believe that this work opens an avenue for the development of solid-state multi-wavelength UV PDs based on wide-band-gap semiconductors.

This work was supported by the Ministry of Science and Technology (Grant Nos. 2011CB302002 and 2009CB929404) of China, the National Science Foundation (Grant Nos. 11174348, 51272280, 11274366, 61204067, 61306011, and 61076007), and the Chinese Academy of Sciences.

- ¹Y. Hou, Z. Mei, and X. Du, *J. Phys. D: Appl. Phys.* **47**, 283001 (2014).
- ²E. Monroy, F. Omnes, and F. Calle, *Semicond. Sci. Technol.* **18**, R33 (2003).
- ³S. Liang, H. Sheng, Y. Liu, Z. Huo, Y. Lu, and H. Shen, *J. Cryst. Growth* **225**, 110–113 (2001).
- ⁴K. Liu, M. Sakurai, and M. Aono, *Sensors* **10**, 8604–8634 (2010).
- ⁵A. Ohtomo, M. Kawasaki, T. Koida, K. Masubuchi, H. Koinuma, Y. Sakurai, Y. Yoshida, T. Yasuda, and Y. Segawa, *Appl. Phys. Lett.* **72**, 2466 (1998).
- ⁶L. Sang, J. Hu, R. Zou, Y. Koide, and M. Liao, *Sci. Rep.* **3**, 2368 (2013).
- ⁷I. Takeuchi, W. Yang, K. S. Chang, M. A. Aronova, T. Venkatesan, R. D. Vispute, and L. A. Bendersky, *J. Appl. Phys.* **94**, 7336 (2003).
- ⁸Z. Zhang, H. V. Wenckstern, M. Schmidt, and M. Grudmann, *Appl. Phys. Lett.* **99**, 083502 (2011).
- ⁹Z. Zhang, H. von Wenckstern, and M. Grudmann, *Appl. Phys. Lett.* **103**, 171111 (2013).
- ¹⁰X. Du, Z. Mei, Z. Liu, Y. Guo, T. Zhang, Y. Hou, Z. Zhang, Q. Xue, and A. Y. Kuznetsov, *Adv. Mater.* **21**, 4625–4630 (2009).
- ¹¹Z. L. Liu, Z. X. Mei, T. C. Zhang, Y. P. Liu, Y. Guo, X. L. Du, A. Hallen, J. J. Zhu, and A. Yu. Kuznetsov, *J. Cryst. Growth* **311**, 4356 (2009).
- ¹²H. L. Liang, Z. X. Mei, Q. H. Zhang, L. Gu, S. Liang, Y. N. Hou, D. Q. Ye, C. Z. Gu, R. C. Yu, and X. L. Du, *Appl. Phys. Lett.* **98**, 221902 (2011).
- ¹³Y. N. Hou, Z. X. Mei, Z. L. Liu, T. C. Zhang, and X. L. Du, *Appl. Phys. Lett.* **98**, 103506 (2011).
- ¹⁴Y. N. Hou, Z. X. Mei, H. L. Liang, D. Q. Ye, S. Liang, C. Z. Gu, and X. L. Du, *Appl. Phys. Lett.* **98**, 263501 (2011).
- ¹⁵Y. N. Hou, Z. X. Mei, H. L. Liang, D. Q. Ye, C. Z. Gu, and X. L. Du, *Appl. Phys. Lett.* **102**, 153510 (2013).
- ¹⁶H. Liang, Z. Mei, Y. Hou, S. Liang, Z. Liu, Y. Liu, J. Li, and X. Du, *J. Cryst. Growth* **381**, 6 (2013).
- ¹⁷A. Janotti and C. G. Van de Walle, *Rep. Prog. Phys.* **72**, 126501 (2009).
- ¹⁸Y. Hou, Z. Mei, H. Liang, D. Ye, C. Gu, X. Du, and Y. Lu, *IEEE Trans. Electron Devices* **60**, 3474 (2013).
- ¹⁹S. Lany and A. Zunger, *Phys. Rev. B* **72**, 035215 (2005).
- ²⁰A. Janotti and C. G. Van de Walle, *Phys. Rev. B* **75**, 121201(R) (2007).
- ²¹H. L. Shi and Y. Duan, *Eur. Phys. J. B* **66**, 439–444 (2008).
- ²²L. Dong and S. P. Aplay, *J. Appl. Phys.* **111**, 113714 (2012).